

Ab initio prediction of ground-state magnetic ordering and high-pressure magnetic phase transition of uranium mononitride

Jing-Jing Zheng(郑晶晶), Yuxi Chen(陈禹西), Chengxiang Zhao(赵承祥), Junfeng Zhang(张均锋), Ping Zhang(张平), Bao-Tian Wang(王保田), and Jiang-Jiang Ma(马江将)

Citation: Chin. Phys. B, 2025, 34 (**8**): 087101. DOI: 10.1088/1674-1056/add4e6
http://cpb.iphy.ac.cn; http://iopscience.iop.org/cpb

What follows is a list of articles you may be interested in

Momentum-dependent anisotropy of the charge density wave gap in quasi-1D $ZrTe_{3-x}Se_x$ (x = 0.015)

Renjie Zhang(张任杰), Yudong Hu(胡裕栋), Yiwei Cheng(程以伟), Yigui Zhong(钟益桂), Xuezhi Chen(陈学智), Junqin Li(李俊琴), Kozo Okazaki, Yaobo Huang(黄耀波), Tian Shang(商恬), Shifeng Jin(金士锋), Baiqing Lv(吕佰晴), and Hong Ding(丁洪)

Chin. Phys. B, 2025, 34 (**7**): 077106. DOI: 10.1088/1674-1056/addcc5

Impact of epitaxial structural parameters on two-dimensional hole gas properties in p-GaN/AlGaN/GaN heterostructures

Fuzhou Wen(文福洲), Qianshu Wu(吴千树), Jinwei Zhang(张津玮), Zhuoran Luo(罗卓然), Senyuan Xu(许森源), Hao Jiang(江灏), and Yang Liu(刘扬)

Chin. Phys. B, 2025, 34 (**7**): 077105. DOI: 10.1088/1674-1056/adc97e

A two-stage injection locking amplifier based on a cavity magnonic oscillator

Mun Kim, Chunlei Zhang, Chenyang Lu, Jacob Burgess, and Can-Ming Hu

Chin. Phys. B, 2025, 34 (**6**): 067104. DOI: 10.1088/1674-1056/add1bf

Amorphous IGMO/IGZO heterojunction thin-film transistors with enhanced ultraviolet detection performance

Jichun Yao(姚继春), Yiyu Zhang(张怡宇), and Xingzhao Liu(刘兴钊)

Chin. Phys. B, 2025, 34 (**5**): 057104. DOI: 10.1088/1674-1056/adb8b6

Electronic structure and disorder effect of $La_3Ni_2O_7$ superconductor

Yuxin Wang(王郁欣), Yi Zhang(张燚), and Kun Jiang(蒋坤)

Chin. Phys. B, 2025, 34 (**4**): 047105. DOI: 10.1088/1674-1056/adbacc

---

SPECIAL TOPIC — Structures and properties of materials under high pressure

Ab initio prediction of ground-state magnetic ordering and high-pressure magnetic phase transition of uranium mononitride

Jing-Jing Zheng(郑晶晶)[1,†], Yuxi Chen(陈禹西)[2,†], Chengxiang Zhao(赵承祥)[2], Junfeng Zhang(张均锋)[3,‡], Ping Zhang(张平)[4], Bao-Tian Wang(王保田)[5], and Jiang-Jiang Ma(马江将)[2§]

[1] *Department of Physics, Taiyuan Normal University, Jinzhong* 030619, *China*
[2] *School of Physics and Electronics Engineering, Shanxi Normal University, Taiyuan* 030031, *China*
[3] *College of Physics and Electronic Engineering, Hainan Normal University, Haikou* 571158, *China*
[4] *Institute of Applied Physics and Computational Mathematics, Beijing* 100088, *China*
[5] *Institute of High Energy Physics, Chinese Academy of Science, Beijing* 100049, *China*

(Received 18 March 2025; revised manuscript received 23 April 2025; accepted manuscript online 7 May 2025)

The ground-state magnetic ordering of uranium mononitride (UN) remains a contentious topic due to the unexpected lack of crystallographic distortion in the traditionally accepted 1$\boldsymbol{k}$ antiferromagnetic (AFM) state. This discrepancy casts doubt on the validity of the 1$\boldsymbol{k}$ magnetic ordering of UN. Here, we investigate the crystal structure, high-pressure phase transitions, and dynamical and mechanical properties of UN in its 1$\boldsymbol{k}$ and 3$\boldsymbol{k}$ AFM ground states using density functional theory (DFT). Our results reveal that the undistorted 3$\boldsymbol{k}$ AFM state of $Fm\bar{3}m$ within the DFT + U + SOC scheme is more consistent with experimental results. The Hubbard U and spin–orbit coupling (SOC) are critical for accurately capturing the crystal structure, high-pressure structural phase transition, and dynamical properties of UN. In addition, we have identified a new high-pressure magnetic phase transition from the nonmagnetic (NM) phase of $R\bar{3}m$ to the $P6_3/mmc$ AFM state. Electronic structure analysis reveals that the magnetic ordering in the ground state is primarily linked to variations in partial 5f orbital distributions. Our calculations provide valuable theoretical insights into the complex magnetic structures of a typical strongly correlated uranium-based compound. Moreover, they provide a framework for understanding other similar actinide systems.

Keywords: UN, antiferromagnetic, magnetic order, density functional theory

PACS: 71.15.Mb, 71.27.+a, 75.30.−m, 75.40.Cx

DOI: 10.1088/1674-1056/add4e6 **CSTR:** 32038.14.CPB.add4e6

1. Introduction

Uranium mononitride (UN) is a promising candidate for the next-generation nuclear fuel in light water reactors (LWRs) due to its superior physical properties compared to today's oxide fuels.[1–3] These properties, including high fissile density, high thermal conductivity, and high melting temperature, are attributed to UN's unique electronic structure, which arises from its partially filled f orbits.[4–6] Notwithstanding the extensive research into its atomic structure, its magnetic structure is another interesting topical issue.[7,8]

In 1965, Curry reported an antiferromagnetic (AFM) structure with a Néel temperature of $T_N = 53$ K.[9] Subsequent experiments confirmed this AFM behavior and classified UN as possessing the 1$\boldsymbol{k}$ (one wave vector) phase.[1,10,11] However, the expected crystallographic distortion associated with the imbalanced magnetic forces in the 1$\boldsymbol{k}$ AFM form was rarely observed. The presence of tetragonal distortion in UN has been a topic of debate for a long time. Marples *et al.*[12] reported a small tetragonal distortion ($\delta = |c/a - 1| = 6.5 \times 10^{-4}$) below the Néel temperature using x-ray diffraction. However, Knott *et al.*[13] did not observe any distortions in single crystals, casting doubt on the proposed 1$\boldsymbol{k}$ ordering. Recently, Bright *et al.*[14] also challenged the 1$\boldsymbol{k}$ AFM state by studying thin epitaxial films of UN. They proposed that the accepted 1$\boldsymbol{k}$ AFM magnetic ground configuration of UN may be incorrect and that the true state of the magnetic configuration should be 3$\boldsymbol{k}$ (three independent wave vectors), which implies that tetragonal distortion does not actually occur. The debate about magnetic ordering is not unique to UN. A similar debate regarding the magnetic state of UO_2 has also emerged.[15–18] Ultimately, neutron inelastic experiments definitively confirmed the presence of a 3$\boldsymbol{k}$ AFM structure.[19]

In addition, theoretical studies play a crucial role in understanding the behavior of 5f electrons and predicting the magnetic properties of actinide compounds such as UN.[20–29] In recent years, extensive first-principles calculations have been performed on UN, investigating the impact of magnetic ordering on its crystal and magnetic structures. Gryaznov *et*

†These authors contributed equally to this work.
‡Corresponding author. E-mail: zhangjf@hainnu.edu.cn
§Corresponding author. E-mail: majiangjiang@sxnu.edu.cn

© 2025 Chinese Physical Society and IOP Publishing Ltd. All rights, including for text and data mining, AI training, and similar technologies, are reserved.

al.[30] used DFT + U simulations to calculate the lattice constants of UN for both ferromagnetic (FM) and 1$\boldsymbol{k}$ AFM orders. They found that the symmetry reduction caused by the tetragonal distortion was inevitable. Utilizing an identical computational method, Lan *et al*.[31] derived $\delta = 0.022$, which substantially exceeds the experimentally measured value of 6.5×10^{-4}.[12] Kocevski *et al*.[32] investigated the crystal structure of UN in 1$\boldsymbol{k}$ AFM ordering, confirming significant distortion induced by the AFM state. It is evident that theoretical calculations performed using 1$\boldsymbol{k}$ AFM ordering consistently demonstrate the expected structural distortion. The divergence between theoretical predictions and experimental findings for the 1$\boldsymbol{k}$ AFM state raises a further question about the magnetic structure of UN. To reconcile this discrepancy, Kocevski *et al*.[2] employed a constrained cubic lattice model for the 1$\boldsymbol{k}$ AFM phase. By constraining the lattice to maintain cubic symmetry, they found that the phonon spectrum no longer exhibited imaginary frequencies, indicating dynamical stability. This suggests that lattice distortion is responsible for the dynamical instability in the 1$\boldsymbol{k}$ AFM state. This discrepancy between theory and experiment may be attributed to two main possibilities. First, as hypothesized by Oglobliche*v et al*.,[1] the current theoretical framework may not adequately capture the complex electronic and magnetic structure of UN. Alternatively, as suggested by Bright *et al*.,[14] the accepted 1$\boldsymbol{k}$ AFM ordering might be incorrect. The true magnetic state of UN could be the 3$\boldsymbol{k}$ AFM state, which would explain the absence of the predicted distortion.

The accurate inclusion of magnetic ordering in DFT calculations is critical for reproducing experimentally observed structural phase transition pressures. For instance, Olsen *et al*.[33] and Bihan *et al*.[34] experimentally observed a UN structural phase transition from the cubic phase to the rhombohedral phase at 28–29 GPa. Previous DFT studies using nonmagnetic (NM) models[35] predicted a transition pressure of 18 GPa, which underestimated the experimentally observed value of 28–29 GPa. After incorporating the 1$\boldsymbol{k}$ AFM ordering into DFT + U calculations,[36] the predicted transition pressure was elevated to 23.5 GPa, bringing it closer to the experimental value. This discrepancy emphasizes the crucial role of magnetic effects. These results also predicted that the pressure-induced structural transition of UN may involve an AFM-to-NM transition. However, the focus of previous theoretical investigations has primarily been the 1$\boldsymbol{k}$ AFM state due to its historical acceptance. Very few theoretical studies have reported details of the 3$\boldsymbol{k}$ AFM ordering. Since UN's physical properties are intimately linked to its magnetic structures, investigating its behavior under 3$\boldsymbol{k}$ AFM ordering is crucial. Exploring the 3$\boldsymbol{k}$ magnetic ground state, pressure-induced structural phase transitions, and their associated physical properties is crucial for understanding this vital nuclear fuel.

In this paper, we present a comprehensive and systematic DFT study that aims to examine the magnetic ground state of UN, exploring both the 1$\boldsymbol{k}$ and 3$\boldsymbol{k}$ AFM configurations. To account for the strong correlations of the U-5f electrons, we employ DFT + U calculations with and without the inclusion of spin–orbit coupling (SOC). We calculate the structural parameters, phonon dispersion relations, and mechanical properties to assess the relative influence of the relativistic effects of SOC on the AFM magnetic ordering. Additionally, considering the impact of magnetic ordering on pressure-induced phase transitions, we perform a thorough structural search of UN at pressures of up to 200 GPa to identify potential structural phase transitions and calculate the transition pressures for various ground-state magnetic orderings. The framework of this paper is as follows. In Section 2, we introduce our calculation method. In Section 3, we present the results and discuss the magnetic ground structure, structural phase transitions, dynamical properties, mechanical properties, and electronic structures. Finally, in Section 4, we summarize our main findings.

2. Methodology

We performed DFT calculations using the projector augmented wave (PAW) method, as implemented in the Vienna *Ab initio* Simulation Package (VASP).[37–40] The generalized gradient approximation (GGA) scheme, as formulated by Perdew, Burke and Ernzerhof (PBE), was chosen to describe the exchange–correlation energy.[41,42] The $6p^6 6d^2 5f^2$ and $2s^2 2p^3$ shells were treated as the valence electrons for U and N, respectively. The conventional cubic cell was selected for the ground-state structural mode in the 1$\boldsymbol{k}$ and the 3$\boldsymbol{k}$ AFM orderings. In all cases, we used a cutoff energy of 520 eV for the plane wave basis set and a Monkhorst–Pack k-point interval of 0.03 Å^{-1} for all phases.[43] The convergence criteria for energy and force were set to 10^{-8} eV and 10^{-4} eV·Å^{-1}, respectively. The strongly correlated 5f electrons of U were described using the DFT + U method formulated by Dudarev *et al*.[44] The screening of Hubbard U was estimated using the DFT calculations presented in Section 3. Phonon calculations were performed using the PHONOPY code[45] and density functional perturbation theory (DFPT) as implemented in VASP.

The particle swarm optimization (PSO) method, as implemented in the CALYPSO code, was used to explore the crystal structure and determine the stable structure of UN at various pressures.[46,47] This method has successfully been employed to predict the high-pressure structure of, for example, hydride systems[48–50] and uranium oxides.[51,52] In the UN structural search, we set the number of generations to 30, with each generation comprising 30 structures. To ensure the stochasticity of the structural search process, the algorithm was de-

signed to update 60% of the structure deterministically, while the remaining 40% was generated through random processes. These searches utilized DFT + U calculations exclusively. After identifying the lower enthalpy phases, we conducted comprehensive structural optimizations and total energy calculations for each candidate in the NM, FM, and AFM states. The pool of structures included both those predicted in this work and previously reported phases from the literature.[33–36]

3. Results and discussion

3.1. The selection of Hubbard U parameters

The DFT + U method is essential for accurately describing the strongly correlated electronic structure of UN, which contains partially filled 5f electron orbitals. The introduction of the Hubbard U parameter within the DFT + U framework enhances the description of localized electronic states. In the case of UN, the selection of an appropriate U value is critical, as it directly impacts key properties such as electronic structures, magnetic moments, equilibrium lattice constants, and formation energies. Determining an optimal Hubbard U parameter is a crucial step to ensure the accuracy of DFT + U simulations, particularly when predicting the ground-state magnetic structure of UN. Therefore, we first focus on selecting suitable U parameters to describe the various magnetic states of UN. The optimal value of the U parameter is primarily determined by comparing theoretical predictions with experimental observations for UN. Specifically, (I) UN exhibits an AFM ground state at low temperatures,[9] (II) UN crystallizes in a rock-salt structure with a lattice constant of 4.889 Å,[9,34,53] (III) UN shows no significant tetragonal distortion[1,10,11] or only a very small tetragonal distortion,[12] and (IV) the experimentally measured magnetic moment of UN is 0.75μ_B.[9]

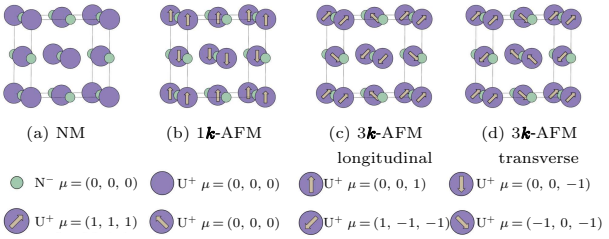


Fig. 1. The magnetic structures of UN in the (a) FM, (b) 1$\boldsymbol{k}$ and (c)–(d) 3$\boldsymbol{k}$ AFM magnetic states. For the 3$\boldsymbol{k}$ AFM state, both the (c) longitudinal and (d) transverse domains are considered. The orientation of the effective magnetic moment (μ) of each ion is described by the $\mu = (a, b, c)$ wave vector matrix. The arrows within the purple spheres indicate the corresponding wave vectors for each magnetic ordering.

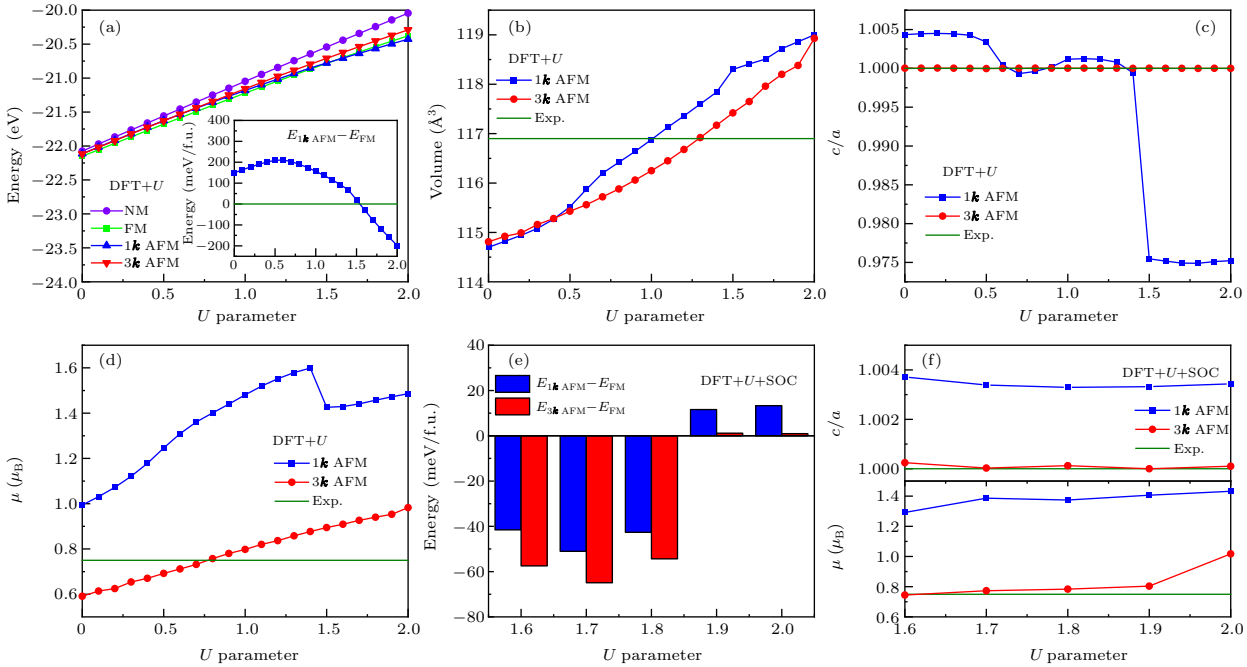


Fig. 2. The total energies (a), the volumes per conventional unit cell (b), the ratios of lattice parameters c/a (c), and the spin magnetic moments of U atoms (d) for the 1$\boldsymbol{k}$ and 3$\boldsymbol{k}$ AFM magnetic states as a function of the U parameter. The green lines represent experimental values.

To investigate the most stable magnetic ground state structure of UN, we calculated the energies of the NM, FM, and AFM states for different U values. The FM, 1$\boldsymbol{k}$ and 3$\boldsymbol{k}$ AFM structures are illustrated in Fig. 1. The energies, unit cell volumes, c/a ratios, and magnetic moments of these magnetic states are shown in Fig. 2. as functions of the U parameter (ranging from 0 to 2.0 eV). First, we investigated the influence of the Hubbard U parameter on the magnetic configurations of UN using DFT + U without SOC. As shown in Figs. 2(a)–2(d), the choice of U has an important influence on these basic properties. In Fig. 2(a), we find that the FM and 1$\boldsymbol{k}$ AFM magnetic states exhibit lower energies compared to the NM

and 3$\boldsymbol{k}$ AFM states. For U values below 1.6 eV, the FM state is the most stable magnetic structure. However, as the U value increases beyond 1.6 eV, the 1$\boldsymbol{k}$ AFM state becomes energetically more favorable than the FM state, indicating that a sufficiently strong on-site Coulomb repulsion is crucial to stabilize the 1$\boldsymbol{k}$ AFM order. In contrast, the 3$\boldsymbol{k}$ magnetic state consistently remains higher in energy than the FM and 1$\boldsymbol{k}$ AFM states, indicating that this configuration is an unstable magnetic ground state within the DFT + U framework.

The calculated equilibrium volumes increase with rising values of U, as illustrated in Fig. 2(b). In the 1$\boldsymbol{k}$ state, U = 0.9 eV reproduces the experimental volume, while U = 1.4 eV yields the best agreement for the 3$\boldsymbol{k}$ state. The c/a ratio for the 1$\boldsymbol{k}$ state (Fig. 2(c)) shows significant variation with U, matching experimental observations only within the range of 0.5–1.3 eV. In contrast, the 3$\boldsymbol{k}$ state displays negligible variation in the c/a ratio, indicating the absence of lattice distortions. Importantly, while specific U values within the 1$\boldsymbol{k}$ state can yield experimental volumes and minor lattice distortions, they fail to predict the AFM ground state observed at low temperatures. Furthermore, magnetic moment calculations, as shown in Fig. 2(d), reveal that the 1$\boldsymbol{k}$ state consistently overestimates experimental values regardless of the choice of U. Similarly, the 3$\boldsymbol{k}$ state can reproduce experimental lattice constants and magnetic moments at particular U values, but it also fails to satisfy the low-temperature AFM ground-state criterion.

SOC is known to have a significant effect on the energy and magnetic moments of ground states. Therefore, we calculated the relative energies of the AFM and FM states, the c/a ratio, and the spin magnetic moment as functions of the U parameter, ranging from 1.6 eV to 2.0 eV (Figs. 2(e) and 2(f)). Specifically, for the 3$\boldsymbol{k}$ AFM state, the energy becomes lower than that of the FM state within the U range of 1.6–1.8 eV, indicating the stability of the AFM phase in this region. The calculated c/a ratio and spin magnetic moment for the 3$\boldsymbol{k}$ AFM state with SOC demonstrate better agreement with experimental values than the 1$\boldsymbol{k}$ state.

Based on these considerations, we selected U = 1.7 eV, as it provides a reasonable balance between satisfying the requirement of an AFM ground state and maintaining a reasonable agreement with experimental lattice parameters and magnetic moments. While this choice may introduce minor deviations in the magnetic moment and lattice constants, it remains a suitable compromise for our study. For the 3$\boldsymbol{k}$ magnetic state, U = 1.7 eV not only ensures that the AFM state is the ground state but also predicts small tetragonal distortion and magnetic moments close to experimental values with the DFT + U + SOC method. Furthermore, U = 1.7 eV is close to the values employed in many previous theoretical studies, such as 1.85 eV,[30] 1.9 eV,[32] and 2.0 eV.[36]

3.2. Magnetic ground-state structure

The crystal structure of UN is known to be influenced by its magnetic ordering. Existing experimental studies of the AFM structure primarily focus on the crystallographic distortion caused by the unbalanced magnetic forces.[12–14] To accurately describe the ground-state magnetic ordering, we investigate the 1$\boldsymbol{k}$ and 3$\boldsymbol{k}$ AFM configurations using various DFT methods, including DFT + U with and without the inclusion of SOC. To facilitate a more accurate comparison with experimental values, two scenarios are considered for the 1$\boldsymbol{k}$ AFM configuration: one constrained to a cubic structure, labeled 1$\boldsymbol{k}$ (I), and another without the cubic constraint, labeled 1$\boldsymbol{k}$ (II). The transverse and longitudinal orientations of the 3$\boldsymbol{k}$ magnetic state are labeled 3$\boldsymbol{k}$ (T) and 3$\boldsymbol{k}$ (L), respectively. Note that the initial atomic configurations of these magnetic states are based on the cubic ($Fm\bar{3}m$) structure.

Table 1 presents the calculated lattice parameters, energies per UN unit cell, magnetic moments, and space group numbers of the 1$\boldsymbol{k}$ (I), 1$\boldsymbol{k}$ (II), 3$\boldsymbol{k}$ (L), and 3$\boldsymbol{k}$ (T) states. Experimental results are included in Table 1 for comparison. Consistent with other theoretical studies,[32] tetragonal distortion is observed in the 1$\boldsymbol{k}$ AFM state regardless of the computational methodology utilized for structural optimization. Interestingly, the DFT and DFT + U methods result in opposing compression/extension trends in the z direction, highlighting the significant impact of the Hubbard U parameter on the structural description of UN. When constrained to a cubic structure, the 1$\boldsymbol{k}$ (I) magnetic state no longer exhibits structural distortion, but its energy is higher than that of the 1$\boldsymbol{k}$ (II) magnetic state. This suggests that the 1$\boldsymbol{k}$ AFM state with structural distortion is the theoretically predicted stable configuration.

In contrast to the 1$\boldsymbol{k}$ AFM state, the 3$\boldsymbol{k}$ AFM state results in the expected absence of lattice distortion, aligning with the prediction made by Bright *et al.*[14] Furthermore, SOC introduces a subtle energy split between the transverse and longitudinal orientations of the 3$\boldsymbol{k}$ AFM state, with 3$\boldsymbol{k}$ (L) lying at slightly lower energy. Therefore, unless explicitly stated otherwise, all references to the 3$\boldsymbol{k}$ state in this article pertain to the longitudinal orientation. By comparing the energies of different magnetic orderings, we find that the energy of the 1$\boldsymbol{k}$ magnetic state is lower than that of the 3$\boldsymbol{k}$ AFM state within the DFT + U framework. When SOC effects are considered, the energy of the 3$\boldsymbol{k}$ (L) AFM state becomes lower than that of the 1$\boldsymbol{k}$ state by 0.021 eV. This trend is consistent with the results presented in Fig. 2(e), which demonstrate that the 3$\boldsymbol{k}$ (L) AFM state is more stable than the 1$\boldsymbol{k}$ state in the DFT + U + SOC framework. The significant energy difference resulting from the inclusion of SOC highlights the crucial role of SOC in determining the magnetic ground state of UN.

Table 1. The total energy (eV/cell), lattice parameters (Å), lattice distortion (δ), and magnetic moment (μ_B) of the 1$\boldsymbol{k}$ and 3$\boldsymbol{k}$ AFM states of UN according to different calculation methods.

Magnetic ordering	Method	Energy (eV)	Lattice parameters (Å)			δ	Magnetic moment
			a	b	c		
1$\boldsymbol{k}$ (I)	DFT	−22.112	4.860	4.860	4.860	0.000	0.991
	DFT + U	−20.626	4.910	4.910	4.910	0.000	1.611
	DTF + U + SOC	−23.487	4.960	4.960	4.960	0.000	1.477
1$\boldsymbol{k}$ (II)	DFT	−22.114	4.852	4.852	4.873	0.004	0.994
	DFT + U	−20.639	4.954	4.954	4.829	0.025	1.441
	DTF + U + SOC	−23.593	4.969	4.969	4.918	0.010	1.636
3$\boldsymbol{k}$ (T)	DFT	−22.118	4.860	4.860	4.860	0.000	0.597
	DFT + U	−20.554	4.907	4.907	4.907	0.000	1.006
	DTF + U + SOC	−23.572	4.961	4.961	4.961	0.000	0.789
3$\boldsymbol{k}$ (L)	DFT	−22.118	4.860	4.860	4.860	0.000	0.596
	DFT + U	−20.537	4.904	4.904	4.904	0.000	0.929
	DTF + U + SOC	−23.614	4.952	4.952	4.952	0.000	0.747
	Exp.[34,53]	–	4.889	4.889	4.889	0.000	0.750

In terms of the magnetic moment, the value of 0.747μ_B predicted by DFT + U + SOC is in excellent agreement with the experimental measurement of 0.750μ_B.[9] Based on the combination of lowest energy, minimal lattice distortion, and good agreement with experimental magnetic moments, we conclude that the 3$\boldsymbol{k}$ AFM state calculated using the DFT + U + SOC method represents the most likely ground state of UN.

3.3. Phase transitions

To investigate the influence of magnetic ordering on high-pressure phase transitions, we performed *ab initio* structural prediction calculations using the DFT + U method over a pressure range of 0–200 GPa. These searches identified several low-enthalpy candidate phases, including $Fm\bar{3}m$, $R\bar{3}m$, and $P6_3/mmc$. Subsequently, we recalculated the formation enthalpies of each structure for NM, FM, and AFM magnetic configurations, employing both DFT + U and DFT + U + SOC methods. For the AFM state, both the 1$\boldsymbol{k}$ (II) and 3$\boldsymbol{k}$ magnetic orders were considered. The enthalpy difference curves relative to the $Fm\bar{3}m$ AFM phase are shown in Fig. 3. Our results reveal that the first high-pressure structural phase transition in UN occurs from $Fm\bar{3}m$ to $R\bar{3}m$, regardless of the initial magnetic ordering or computational approach. This phase transition contrasts with both experimental observations and other theoretical results.[36] Furthermore, we find that

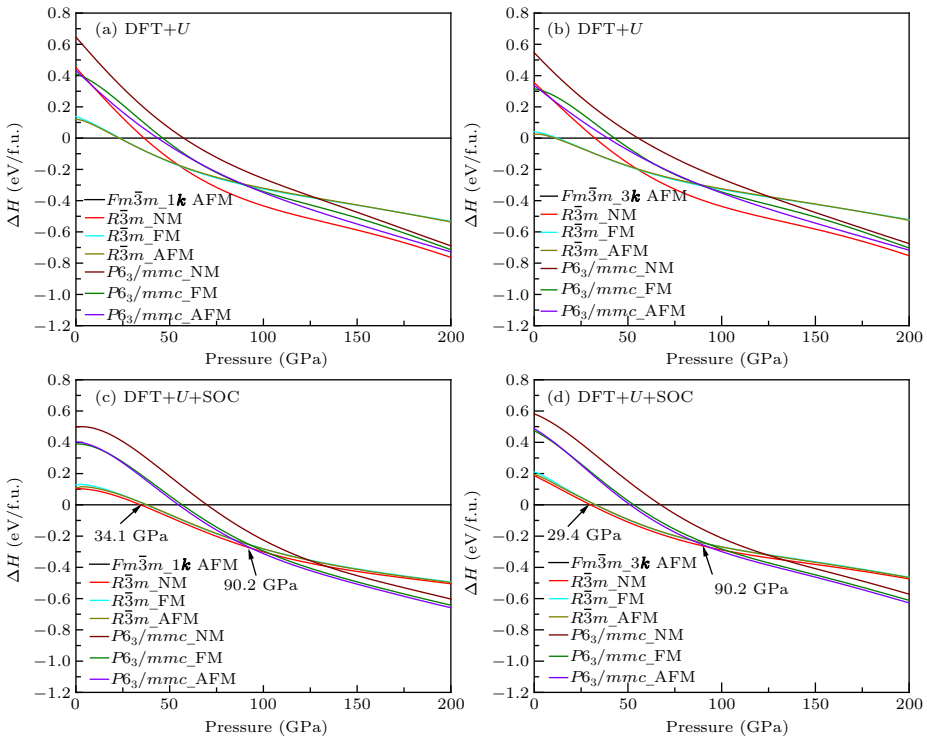


Fig. 3. Pressure dependence (0–200 GPa) of the relative enthalpy for the (a) 1$\boldsymbol{k}$ and (b) 3$\boldsymbol{k}$ magnetic states calculated using DFT + U, and for the (c) 1$\boldsymbol{k}$ and (d) 3$\boldsymbol{k}$ magnetic states calculated using DFT + U + SOC. The enthalpy of the $Fm\bar{3}m$ AFM phase is the zero reference.

the incorporation of SOC leads to a phase transition pressure more consistent with experimental findings, emphasizing the crucial role of SOC. The transition pressures are also influenced by the magnetic ordering. For the 1$\boldsymbol{k}$ (II) AFM state, the DFT + U + SOC method predicts a transition pressure of 34.1 GPa, slightly higher than the previously reported value.[36] Conversely, the predicted transition pressure for the 3$\boldsymbol{k}$ AFM state is 29.4 GPa, providing a closer match to experimental observations of UN's structural phase transition behavior.[33,34] With increasing pressure, we observe that according to DFT + U + SOC, the 1$\boldsymbol{k}$ (II) and 3$\boldsymbol{k}$ magnetic states undergo a second structural phase transition from the $R\bar{3}m$ NM phase to the $P6_3/mmc$ AFM phase at 90.2 GPa. Notably, this transition does not occur without SOC, clearly demonstrating the significant influence of SOC on pressure-induced structural transitions.

Figure 4 illustrates the primitive cells and supercells of these three phases. The $R\bar{3}m$ phase exhibits a lattice parameter of 3.489 Å at 40 GPa. The unit cell of the $P6_3/mmc$ phase contains two formula units (f.u.) of UN, with lattice constants of $a = b = 2.982$ Å and $c = 6.025$ Å at 91 GPa.

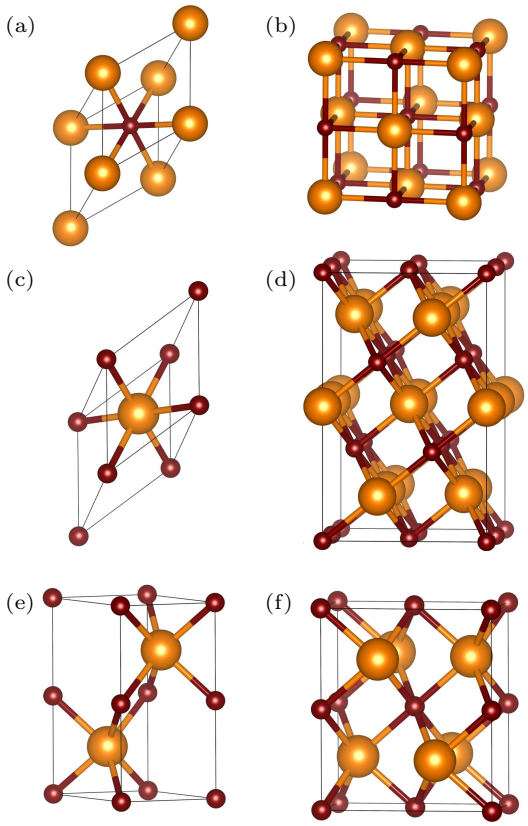


Fig. 4. Crystal structures of (a), (c), (e) the primitive cells and (b), (d), (f) the supercells of the $Fm\bar{3}m$, $R\bar{3}m$, and $P6_3/mmc$ phases of UN, respectively. Here, the large orange and small brown spheres represent U and N atoms, respectively.

3.4. Dynamical and mechanical stability

To further validate our method and assess the stability of UN in the 1$\boldsymbol{k}$ (I), 1$\boldsymbol{k}$ (II), and 3$\boldsymbol{k}$ AFM magnetic ground states, we also analyze their dynamic and mechanical properties. The DFT + U and DFT + U + SOC methods are employed to calculate the phonon dispersion relations of the $Fm\bar{3}m$ AFM, $R\bar{3}m$ NM, and $P6_3/mmc$ AFM phases at their respective stable pressure points. A primitive cell containing two atoms is used for the $Fm\bar{3}m$ and $R\bar{3}m$ phases, while the primitive cell of the $P6_3/mmc$ phase contains four atoms. The calculated phonon dispersion relations for UN at the corresponding pressures are displayed in Fig. 5. For the $Fm\bar{3}m$ phase, the results of a previous experimental investigation[54] are plotted for comparison. The calculated phonon dispersion relations consist of six total modes, including three acoustic modes in the low-frequency zone and three optical modes in the high-frequency zone. Due to the large mass difference between the U and N atoms, there is a large gap between the optical modes and the acoustic modes. The optical modes show nearly flat dispersion. Similar features have also been observed in UC,[55] PuH_2,[56] ThH_2,[57] and ThN.[58]

As shown in Figs. 5(a) and 5(b), the constrained cubic structure 1$\boldsymbol{k}$ (I) phase exhibits phonon dispersion that closely matches the experimental results,[54] both with and without SOC. The absence of imaginary frequencies confirms the dynamical stability of the cubic 1$\boldsymbol{k}$ (I) phase. However, the 1$\boldsymbol{k}$ (II) phase, which undergoes lattice distortion, shows dynamical instability regardless of whether SOC is considered. These findings are consistent with the computational results of Kocevski *et al.*[2] and indicate that the distorted lattice structure is unstable, likely due to symmetry breaking caused by the structural distortion. For the 3$\boldsymbol{k}$ AFM magnetic ground state, dynamical instability is observed without SOC, as shown in Fig. 5(a). However, when SOC is included, the 3$\boldsymbol{k}$ AFM state becomes dynamically stable, as confirmed by its phonon spectrum. The low-frequency phonon branches agree well with experimental data, while the high-frequency optical branches have slightly lower vibration frequencies than those observed experimentally. This discrepancy may be due to the fact that the lattice constants predicted by DFT + U + SOC are slightly larger than the experimental values. Based on the combination of magnetic ordering and lattice distortion, we conclude that the 1$\boldsymbol{k}$ (I) and 3$\boldsymbol{k}$ AFM phases calculated using the DFT + U + SOC method represent the most likely ground state of UN.

For the high-pressure $R\bar{3}m$ NM and $Fm\bar{3}m$ AFM phases, the inclusion of SOC has a limited impact on the low-frequency acoustic phonon branches, as shown in Figs. 5(c) and 5(d). The primary effect of SOC is a reduction in the vibrational frequencies of the high-frequency optical branches. With increasing pressure, the highest vibrational frequencies of the high-pressure phase exceed those of the low-pressure phase, indicating that pressure enhances the interaction between cations and anions.

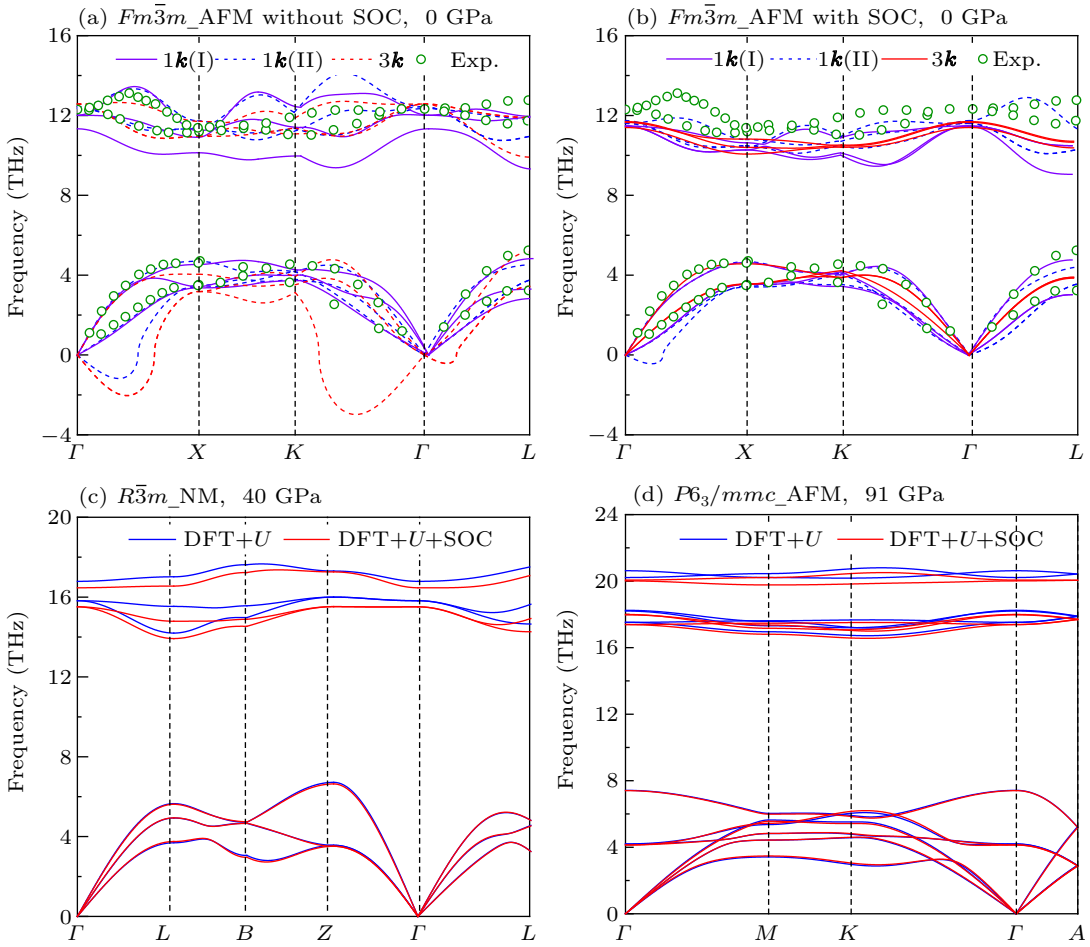


Fig. 5. Calculated phonon dispersion relations for the $Fm\bar{3}m$ structure with 1$\boldsymbol{k}$ (I), 1$\boldsymbol{k}$ (II), and 3$\boldsymbol{k}$ magnetic ordering in the AFM phase at 0 GPa using DFT + U without (a) and with SOC (b). Previous results from an inelastic scattering experiment with thermal neutrons (circles)[54] for the 1$\boldsymbol{k}$ AFM phase are also shown for comparison. The phonon dispersion relations for (c) the $R\bar{3}m$ structure in the NM phase at 40 GPa and (d) the $P6_3/mmc$ structure in the AFM phase at 91 GPa.

Table 2. The elastic constants (GPa), bulk moduli B (GPa), Young's moduli E (GPa), shear moduli G (GPa), Vickers hardnesses H_v (GPa), Poisson ratios ν, and Debye temperatures Θ_D (K) of UN for the $Fm\bar{3}m$ structure in the 1$\boldsymbol{k}$ (I), 1$\boldsymbol{k}$ (II), and 3$\boldsymbol{k}$ AFM states at 0 GPa, the $R\bar{3}m$ structure in the NM state at 40 GPa, and the $P6_3/mmc$ structure in the AFM state at 91 GPa.

	DFT + U			DFT + U+SOC					Exp.
	$Fm\bar{3}m$ AFM			$Fm\bar{3}m$ AFM			$R\bar{3}m$	$P6_3/mmc$	$Fm\bar{3}m$
	1$\boldsymbol{k}$ (I)	1$\boldsymbol{k}$ (II)	3$\boldsymbol{k}$	1$\boldsymbol{k}$ (I)	1$\boldsymbol{k}$ (II)	3$\boldsymbol{k}$	NM	AFM	[61]
C_{11}	395.2	421.4	395.2	363.5	357.1	365.5	376.7	603.4	423.9
C_{12}	92.7	85.6	96.0	92.8	88.0	94.6	172.7	300.7	98.1
C_{13}	–	109.0	–	–	101.4	–	309.8	336.3	–
C_{14}	–	–	–	–	–	–	71.0	–	–
C_{33}	–	341.2	–	–	380.7	–	569.9	943.1	–
C_{44}	57.0	67.5	48.1	61.5	63.5	75.7	188.3	269.2	75.7
C_{66}	–	–	–	–	–	–	97.6	150.2	–
H_v	7.6	6.9	6.9	7.8	7.9	11.0	8.2	16.9	–
B	187.4	198.6	195.7	186.2	186.1	185.0	295.7	444.3	205.9
E	207.9	207.2	205.0	210.0	210.8	245.0	290.8	539.1	229.0
G	79.1	78.1	77.3	80.0	80.4	95.8	108.8	207.7	103.9
ν	0.315	0.326	0.325	0.312	0.311	0.279	0.336	0.298	0.263
Θ_D	322.3	319.5	317.7	324.1	324.8	353.1	366.3	493.6	282.0

Next, we calculate the elastic constants of all our studied structures using DFT + U with and without SOC to assess their mechanical stability and related properties. The calculated elastic constants, various moduli, Vickers hardnesses, Poisson ratios, and Debye temperatures are listed in Table 2. The number of independent elastic tensor terms, C_{ij}, differs between the $Fm\bar{3}m$, $R\bar{3}m$, and $P6_3/mmc$ phases. Additionally, due to the significant structural distortion in the 1$\boldsymbol{k}$ (II) AFM state of the $Fm\bar{3}m$ phase, a direct comparison of its C_{ij} with those of the 3$\boldsymbol{k}$ AFM state is not meaningful. We also calculated various moduli, Vickers hardnesses, Poisson ratios, and Debye temperatures for these structures. The mechanical stability criteria[59,60] for the $Fm\bar{3}m$ structure are $C_{11} - C_{12} > 0$, $C_{11} + 2C_{12} > 0$, and $C_{44} > 0$. The criteria for the $R\bar{3}m$ structure are $C_{11} - C_{12} > 0$, $C_{44} > 0$, $C_{13}^2 < \frac{1}{2} \times C_{33}(C_{11} + C_{12})$, and $C_{14}^2 < \frac{1}{2} \times C_{44}(C_{11} - C_{12})$, while for the $P6_3/mmc$ structure, they are $C_{44} > 0$, $C_{11} > |C_{12}|$, and $(C_{11} + 2C_{12})C_{33} > 2C_{13}^2$. From our calculated elastic constants, it can be concluded that all the structures satisfy the corresponding mechanical stability criteria.

A comparison between the elastic constants of the 1$\boldsymbol{k}$ (I) and 1$\boldsymbol{k}$ (II) phases aims to assess the impact of lattice distortion on the mechanical properties of UN. The elastic constant C_{11}, associated with axial compression, is consistently larger than C_{44} (related to shear deformation), indicating that

all phases exhibit greater resistance to compression than to shear. The difference in C_{11} between the 1$\boldsymbol{k}$ (I) and 1$\boldsymbol{k}$ (II) phases calculated using the DFT + U method is significantly larger than that obtained using DFT + U + SOC, as the latter yields smaller lattice distortions. However, the bulk moduli (B), Young's moduli (E), and shear moduli (G) of the 1$\boldsymbol{k}$ (I) and 1$\boldsymbol{k}$ (II) phases are nearly identical, likely due to the minimal impact of small structural distortions on these moduli. When SOC is included, both the elastic constants and bulk moduli exhibit noticeable changes, underscoring the significant influence of SOC. Compared to the 1$\boldsymbol{k}$ (I) phase without lattice distortion, the 3$\boldsymbol{k}$ AFM state yields results closer to experimental values, as its calculated lattice constants align more closely with experimental data. These findings demonstrate that lattice distortions significantly affect elastic constants, particularly C_{11}. For structures without lattice distortions, the 3$\boldsymbol{k}$ AFM state, calculated using the DFT + U + SOC method, provides a more accurate description of the ground-state mechanical properties of UN. This underscores the significant impact of AFM magnetic ordering and SOC effects on the mechanical properties of UN.

Compared with the ground-state structure, we find that the mechanical properties of UN are significantly enhanced after the pressure-induced structural phase transitions. For example, the Debye temperature Θ_{D} increases with compression pressure from 353.1 K for the 3$\boldsymbol{k}$ AFM state of $Fm\bar{3}m$ under ambient conditions to 493.6 K for the AFM state of $P6_3/mmc$ at high pressure. The preceding analysis indicates that both the ground-state magnetic ordering and the pressure-induced magnetic phase transitions significantly influence the mechanical properties of UN. To gain further insight into the intrinsic nature of these magnetic phases, we conducted a detailed investigation to explore the unique electronic behavior of UN during magnetic phase transformations. This approach has been successfully applied to investigate the magnetic structure of actinide compounds, such as PuO_2.[62]

3.5. Electronic structures

To investigate the intrinsic impact of magnetic ordering on the structure, high-pressure transition, and dynamical and mechanical properties of UN, we performed DFT + U calculations for both spin-polarized and spin-unpolarized cases. Figure 6 presents the total electronic DOSs and the projected densities of states (PDOS) of the 1$\boldsymbol{k}$ (II) and the 3$\boldsymbol{k}$ AFM states. It is evident that both the 1$\boldsymbol{k}$ (II) and 3$\boldsymbol{k}$ AFM states exhibit metallic behavior, with significant contributions from 5f electrons near the Fermi level. The DOSs and the PDOSs of the 1$\boldsymbol{k}$ (II) and 3$\boldsymbol{k}$ $Fm\bar{3}m$ states indicate the significant role of the 5f electrons. As shown in Figs. 6(a) and 6(c), the DFT + U results exhibit several sharp and intense peaks in the DOSs between −0.5 eV and 0.5 eV, indicating localized 5f electronic states. The inclusion of SOC slightly smoothes the peaks near the Fermi level, as shown in Figs. 6(b) and 6(d), suggesting a reduction in the localization of the 5f orbitals. Interestingly, the 5f electronic states exhibit distinct distributions in the 1$\boldsymbol{k}$ (II) and the 3$\boldsymbol{k}$ AFM states, which may be attributed to the crystal structure distortions present in the 1$\boldsymbol{k}$ (II) AFM state.

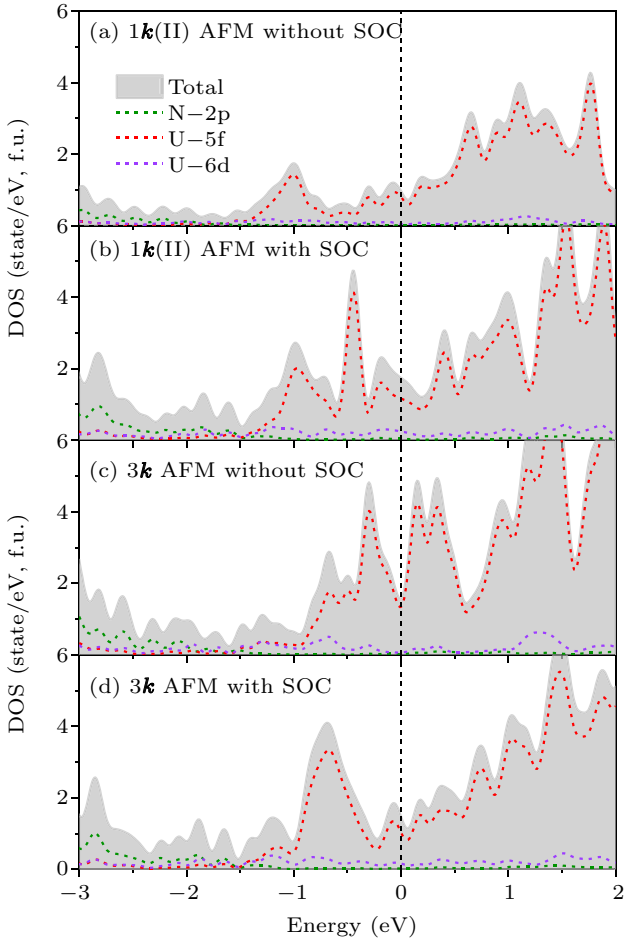


Fig. 6. The total and projected electronic densities of states (DOSs) of UN calculated using DFT + U for the 1$\boldsymbol{k}$ (II) AFM state (a) without and (b) with SOC and for the 3$\boldsymbol{k}$ AFM state (c) without and (d) with SOC. The Fermi level is set to zero, as represented by a vertical dashed line.

It is well known that the octahedral-bonding environment around the U atoms allows the 5f states to split into distinct energy levels: the highest singlet state of A_{2u} (f_{xyz}), the lower two-triplet state of T_{1u} ($f_{y(3x^2-y^2)}$, f_{zx^2}, $f_{x(3y^2-x^2)}$) and T_{2u} (f_{yz^2}, f_{xz^2}, f_{z^3}). The relative energy levels of T_{1u} and T_{2u} depend on the strength of the σ and π bonding interactions.[63] When the σ character predominates, the T_{1u} state is at the lowest energy level. Conversely, the T_{1u} state is at a higher energy level. To gain further insight into the partial 5f orbital distribution, we plotted the PDOSs of 5f orbitals and the electronic band structures of the $f_{y(3x^2-y^2)}$ and f_{zx^2} orbitals in the 1$\boldsymbol{k}$ (II) and 3$\boldsymbol{k}$ AFM states using DFT + U + SOC (as shown in Fig. 7). The PDOS analysis reveals that the f_{zx^2} and $f_{y(3x^2-y^2)}$ orbitals dominate the states below the Fermi level, while the f_{xz^2} and f_{z^3} orbitals are predominant in the states above the Fermi level

in the 1***k*** (II) AFM phase. In contrast, the contributions of the 5f orbitals near the Fermi level are relatively uniform in the 3***k*** AFM state.

To better reveal the distribution characteristics of partial 5f orbitals, we performed a close examination of the band structure. As shown in Fig. 7(a), the $f_{y(3x^2-y^2)}$ and f_{zx^2} orbitals primarily contribute to the valence band (−1.5 eV to 0 eV) in the 1***k*** (II) AFM. In contrast, in the 3***k*** AFM, these orbitals contribute across a broader energy range (from −1.5 eV to 2 eV) near the Fermi surface, as shown in Fig. 7(b). Furthermore, compared to the 1***k*** (II) AFM state, the bands near the Fermi level in the 3***k*** AFM state display splitting and reduced degeneracy.

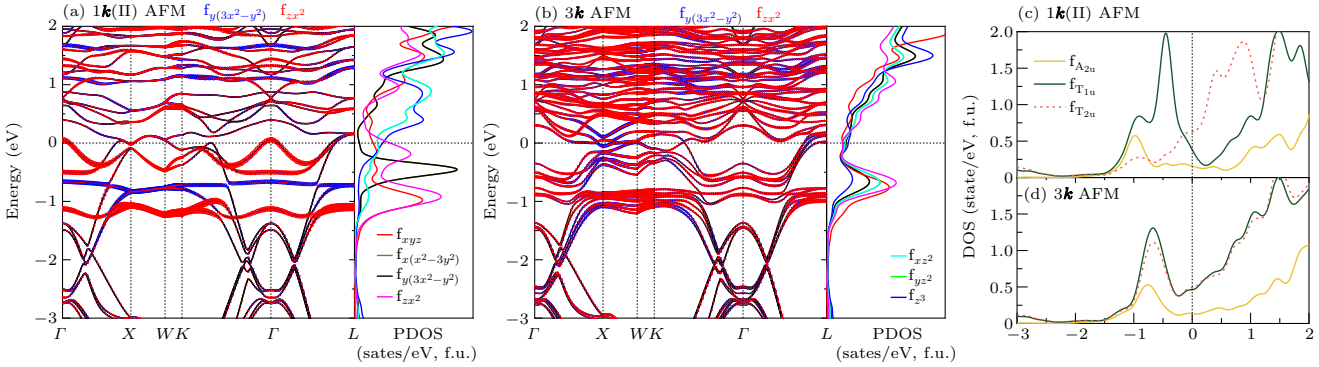


Fig. 7. The PDOS of the U 5f orbitals and $f_{y(3x^2-y^2)}$ and f_{zx^2} orbital-projected band structures of the 1***k*** (II) AFM (a) and the 3***k*** AFM (b) configurations calculated using DFT + U + SOC. The PDOSs associated with the A_{2u}, T_{1u}, and T_{2u} energy levels of the 1***k*** (II) (c) and 3***k*** AFM (d) states of UN, respectively.

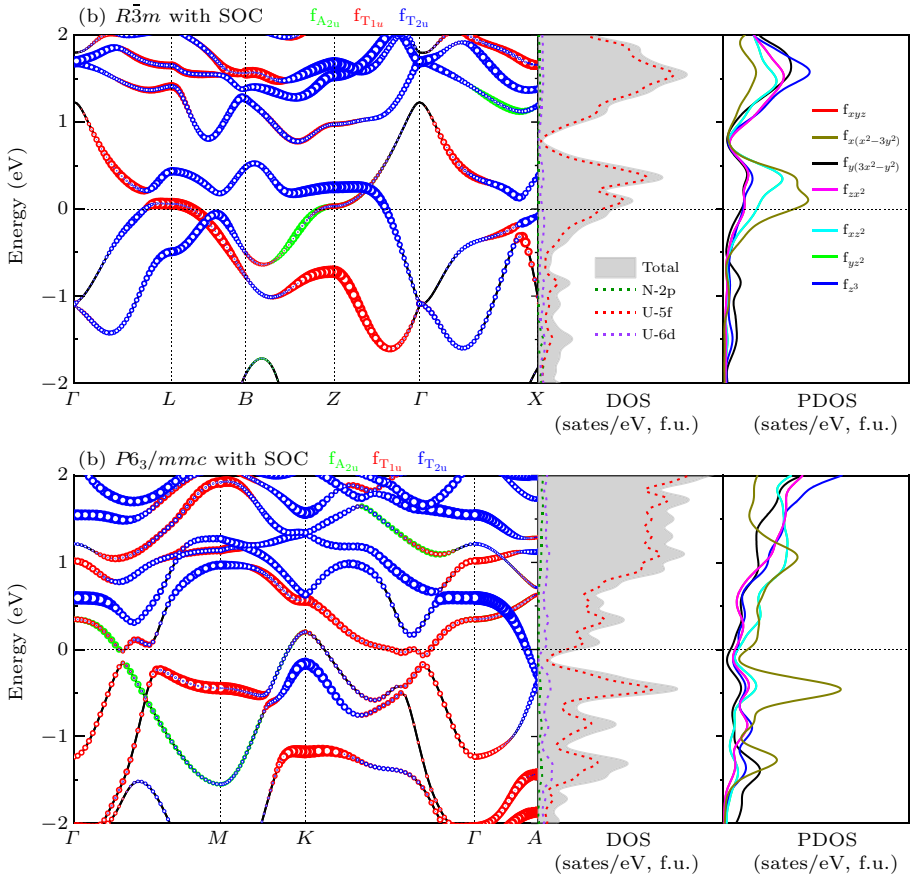


Fig. 8. Calculated A_{2u}-, T_{1u}-, and T_{2u}-level orbital-projected band structures show the DOS and PDOS projected onto the U 5f orbital for (a) $R\bar{3}m$ NM and (b) $P6_3/mmc$ AFM phases under high pressure. The Fermi level is set to zero, as represented by a vertical dashed line.

The differences in the partial distribution of the 5f orbitals may lead to variations in bonding interactions between the 1***k*** (II) and 3***k*** AFM states. To investigate this, we plotted the total DOS for the combined partial 5f orbitals associated with the A_{2u}, T_{1u}, and T_{2u} energy levels of the 1***k*** (II) and 3***k*** AFM states, as shown in Figs. 7(c) and 7(d), respectively. In the energy range of −1.0 eV to −0.2 eV, the 1***k*** (II) AFM state is primarily dominated by contributions from the $f_{T_{1u}}$ orbitals,

while in the range from −0.2 eV to 1 eV, the $f_{T_{2u}}$ orbitals are the main contributors. In contrast, near the Fermi level in the 3$\boldsymbol{k}$ AFM state, the contributions from $f_{T_{1u}}$ and $f_{T_{2u}}$ are nearly equivalent. Based on these differences in partial 5f orbital distribution between the 1$\boldsymbol{k}$ (II) and 3$\boldsymbol{k}$ AFM states, we infer that there may be variations in bonding interactions between the 1$\boldsymbol{k}$ (II) and 3$\boldsymbol{k}$ AFM states of UN.

Subsequently, we further investigated the evolution of the electronic structure during high-pressure-induced magnetic structural phase transitions. The calculated $f_{A_{2u}}$, $f_{T_{1u}}$, and $f_{T_{2u}}$ orbital-projected band structures, projecting the DOS and PDOS onto the 5f orbitals under high pressure, are presented in Fig. 8. It is noteworthy that the $R\bar{3}m$ NM phase of UN exhibits metallic behavior, which strongly correlates with the 5f electrons. In contrast, the $P6_3/mmc$ phase displays semi-metallic characteristics due to the presence of a continuous bandgap between the valence and conduction bands. This transition from metallic to semi-metallic behavior following the high-pressure structural phase transition is consistent with observations of UO_3.[51]

From the band structure analysis, it is evident that the $f_{T_{1u}}$ and $f_{T_{2u}}$ states dominate near the Fermi level in both structures. The DOS analysis indicates that the 5f electrons in the $R\bar{3}m$ NM phase exhibit itinerant features below the Fermi level. In contrast, the 5f electrons in the $P6_3/mmc$ AFM phase show strong localization near the Fermi level. The calculated partial DOS projected onto the U 5f orbitals reveals that the $f_{x(x^2-3y^2)}$ orbital is the primary contributor near the Fermi level for both phases. Notably, the contribution of the $f_{x(x^2-3y^2)}$ orbital shifts to lower-energy regions during the NM-to-AFM transition with increasing pressure. Although the $f_{x(x^2-3y^2)}$ orbital remains the dominant contributor at the Fermi level in the $P6_3/mmc$ AFM phase, its contribution is reduced.

Overall, our findings suggest that the primary partial 5f orbital remains the dominant contributor near the Fermi level in both the $R\bar{3}m$ NM and $P6_3/mmc$ AFM phases. However, the 5f electrons shift to lower-energy regions and become more localized in the $P6_3/mmc$ AFM phase. This relocalization of the 5f electrons may enhance the exchange interactions between uranium atoms, leading to the stabilization of the $P6_3/mmc$ AFM state. These changes in electronic structure may also have significant implications for the dynamical and mechanical properties of UN under high pressure.

4. Conclusion

In this work, we investigated the ground-state magnetic ordering and high-pressure magnetic phase transitions in UN using first-principles calculations. Specifically, we employed the DFT + U + SOC scheme to study the 1$\boldsymbol{k}$ and 3$\boldsymbol{k}$ AFM states, calculating the crystal structure, dynamical properties, mechanical properties, and electronic structure. Through comprehensive structural searches, we successfully reproduced the structural phase transition from the $Fm\bar{3}m$ AFM state to the $R\bar{3}m$ NM state at 29.4 GPa. Furthermore, we predicted a novel pressure-induced magnetic phase transition within the $R\bar{3}m$ NM phase, transforming it to the $P6_3/mmc$ AFM state. Electronic structure analysis revealed that the primary difference between the 1$\boldsymbol{k}$ and 3$\boldsymbol{k}$ AFM states in the $Fm\bar{3}m$ phase lies in their partial 5f orbital distributions. These findings provide valuable insights into the complex interplay between magnetism, structure, and electronic properties in UN and have important implications for understanding the behavior of actinide materials under extreme conditions.

Acknowledgments

Project supported by the National Natural Science Foundation of China (Grant Nos. 12204482 and U2430211), the Scientific and Technological Innovation Programs of Higher Education Institutions in Shanxi (Grant No. 2020L0537), the Fundamental Research Program of Shanxi Province (Grant No. 202103021224250), and the Hainan Provincial Natural Science Foundation of China (Grant No. 225MS076).

References

[1] Ogloblichev V, Verkhovskii S, Mirmelstein A, Piskunov Y, Germov A, Potapov A, Gubkin A and Andreev A 2021 *Phys. Rev. B* **104** 155148
[2] Kocevski V, Cooper M W, Claisse A J and Andersson D A 2022 *J. Nucl. Mater.* **562** 153553
[3] Mishchenko Y, Johnson K D, Jadern as D, Wallenius J and Lopes D A 2021 *J. Nucl. Mater.* **556** 153249
[4] Gorbunov D, Nomura T, Zvyagin A, Henriques M, Andreev A, Skourski Y, Zvyagina G, Troc R, Zherlitsyn S and Wosnitza J 2019 *Phys. Rev. B* **100** 024417
[5] Fujimori S I, Ohkochi T, Okane T, Saitoh Y, Fujimori A, Yamagami H, Haga Y, Yamamoto E and Onuki Y 2012 *Phys. Rev. B* **86** 235108
[6] AbdulHameed M, Beeler B, Galvin C O and Cooper M W 2024 *J. Nucl. Mater.* **600** 155247
[7] Hamann S, Forster T, Gorbunov D I, König M, Uhlarz M, Wosnitza J and Helm T 2021 *Phys. Rev. B* **104** 155123
[8] Sikorski E L, Jaques B J and Li L 2021 *J. Appl. Phys.* **130**
[9] Curry N 1965 *Proc. Phys. Soc.* **86** 1193
[10] Van Doorn C and Du Plessis P D V 1977 *J. Low Temp. Phys.* **28** 391
[11] Marples J 1970 *J. Phys. Chem. Solids* **31** 2431
[12] Marples J, Sampson C, Wedgwood F and Kuznietz M 1975 *J. Phys. C: Solid State Phys.* **8** 708
[13] Knott H, Lander G, Mueller M and Vogt O 1980 *Phys. Rev. B* **21** 4159
[14] Bright E L, Springell R, Porter D, Collins S and Lander G H 2019 *Phys. Rev. B* **100** 134426
[15] Zhou S, Ma H, Xiao E, Gofryk K, Jiang C, Manley M E, Hurley D H and Marianetti C A 2022 *Phys. Rev. B* **106** 125134
[16] Pegg J T, Shields A E, Storr M T, Wills A S, De Leeuw N H and Scanlon D O 2019 *Phys. Chem. Chem. Phys.* **21** 760
[17] Dorado B and Garcia P 2013 *Phys. Rev. B* **87** 195139
[18] Wang B T, Zhang P, Lizarraga R, Di Marco I and Eriksson O 2013 *Phys. Rev. B* **88** 104107
[19] Blackburn E, Caciuffo R, Magnani N, Santini P, Brown P, Enderle M and Lander G 2005 *Phys. Rev. B* **72** 184411
[20] Lu Y, Wang B T, Li R W, Shi H L and Zhang P 2011 *J. Nucl. Mater.* **410** 46
[21] Lu Y, Wang B T, Li R W, Shi H and Zhang P 2010 *J. Nucl. Mater.* **406** 218

[22] Atta-Fynn R and Ray A K 2007 *Phys. Rev. B* **76** 115101
[23] Brooks M and Kelly P 1983 *Phys. Rev. Lett.* **51** 1708
[24] Cooper B R 1982 *J. Magn. Magn. Mater.* **29** 230
[25] Chan S K 1971 *J. Phys. Chem. Solids* **32** 1111
[26] Skriver H L, Andersen O and Johansson B 1980 *Phys. Rev. Lett.* **44** 1230
[27] Brooks M 1984 *J. Phys. F: Met. Phys.* **14** 639
[28] Sedmidubsky D, Konings R and Novak P 2005 *J. Nucl. Mater.* **344** 40
[29] Yin Q, Kutepov A, Haule K, Kotliar G, Savrasov S Y and Pickett W E 2011 *Phys. Rev. B* **84** 195111
[30] Gryaznov D, Heifets E and Kotomin E 2012 *Phys. Chem. Chem. Phys.* **14** 4482
[31] Lan J H, Zhao Z C, Wu Q, Zhao Y L, Chai Z F and Shi W Q 2013 *J. Appl. Phys.* **114**
[32] Kocevski V, Rehn D A, Cooper M W and Andersson D A 2022 *J. Nucl. Mater.* **559** 153401
[33] Olsen J S, Gerward L and Benedict U 1985 *J. Appl. Crystallogr.* **18** 37
[34] Le Bihan T, Idiri M and Heathman S 2003 *J. Alloys Compd.* **358** 120
[35] Modak P and Verma A K 2011 *Phys. Rev. B* **84** 024108
[36] Mei Z G and Stan M 2014 *J. Alloys Compd.* **588** 648
[37] Kresse G and Joubert D 1999 *Phys. Rev. B* **59** 1758
[38] Blochl P E 1994 *Phys. Rev. B* **50** 17953
[39] Kresse G and Hafner J 1994 *J. Phys.: Condens. Matter* **6** 8245
[40] Kresse G and Furthmuller J 1996 *Phys. Rev. B* **54** 11169
[41] Perdew J P and Wang Y 1992 *Phys. Rev. B* **45** 13244
[42] Perdew J P, Burke K and Ernzerhof M 1996 *Phys. Rev. Lett.* **77** 3865
[43] Monkhorst H J and Pack J D 1976 *Phys. Rev. B* **13** 5188
[44] Dudarev S L, Botton G A, Savrasov S Y, Humphreys C and Sutton A P 1998 *Phys. Rev. B* **57** 1505
[45] Togo A, Oba F and Tanaka I 2008 *Phys. Rev. B* **78** 134106
[46] Wang Y, Lv J, Zhu L and Ma Y 2010 *Phys. Rev. B* **82** 094116
[47] Wang Y, Lv J, Zhu L and Ma Y 2012 *Comput. Phys. Commun.* **183** 2063
[48] Wang D, Zhang H, Chen H L, Wu J, Zang Q J and Lu W C 2019 *Phys. Lett. A* **383** 774
[49] Kruglov I A, Kvashnin A G, Goncharov A F, Oganov A R, Lobanov S S, Holtgrewe N, Jiang S, Prakapenka V B, Greenberg E and Yanilkin A V 2018 *Sci. Adv.* **4** eaat9776
[50] Wang X, Li M, Zheng F and Zhang P 2018 *Phys. Lett. A* **382** 2959
[51] Ma J J, Zhang C B, Qiu R, Zhang P, Ao B and Wang B T 2021 *Phys. Rev. B* **104** 174103
[52] Song H X, Geng H Y and Wu Q 2012 *Phys. Rev. B* **85** 064110
[53] Muromura T and Tagawa H 1979 *J. Nucl. Mater.* **79**
[54] Jackman J, Holden T, Buyers W, DuPlessis P D V, Vogt O and Genossar J 1986 *Phys. Rev. B* **33** 7144
[55] Liang R T, Bo T, Yin W Q, Nie C M, Zhang L, Chai Z F and Shi W Q 2023 *Nucl. Eng. Technol.* **55** 2556
[56] Zheng J J, Wang B T, Di Marco I and Li W D 2014 *Int. J. Hydrog. Energy* **39** 13255
[57] Wang B T, Zhang P, Song H, Shi H, Li D and Li W D 2010 *J. Nucl. Mater.* **401** 124
[58] Lu Y, Li D F, Wang B T, Li R W and Zhang P 2011 *J. Nucl. Mater.* **408** 136
[59] Mouhat F and Coudert F X 2014 *Phys. Rev. B* **90** 224104
[60] Nye J F 1985 *Physical Properties of Crystals: Their Representation by Tensors and Matrices* (Oxford University Press)
[61] Salleh M, MacDonald J E, Saunders G and Du Plessis P D V 1986 *J. Mater. Sci.* **21** 2577
[62] Hou Y F, Jiang W, Li S J, Fu Z G and Zhang P 2023 *Chin. Phys. B* **32** 027103
[63] Allen J P and Watson G W 2014 *Phys. Chem. Chem. Phys.* **16** 21016